Supporting Information

Contents

XRD-patterns of ATO-compounds

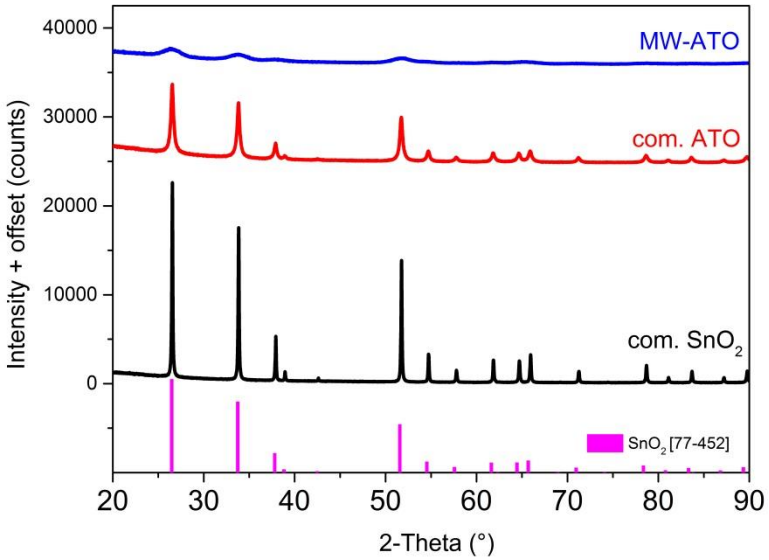

Figure S1. XRD of commercial SnO2 and ATO samples was well as MW-Ir/ATO

Due to the very similar ionic radii of Sn^{IV}, Sb^{III} and Sb^{V} and the broad peaks resulting from small crystalline domains, the obtained XRD-patterns cannot be distinguished from the pure SnO_2-cassiterite.

Conductivities and specific surface areas of ATO

Table S1. Specific surface area and resistivities of commercial powders and samples prepared in the MW at various temperatures.

Compound	ρ [Ω cm]	S_{BET} (m^2 g^{-1})
Comm. SnO_2	$1{,}28.10^4$	7
MW-ATO 180°C	$1{,}92.10^5$	--
MW-ATO 210°C	$1{,}55.10^4$	--
MW-ATO 240°C	$5{,}10.10^4$	--
MW-ATO 270°C	$1{,}71.10^1$	207
MW-ATO 290°C	$1{,}17.10^1$	184
Commercial ATO	$2{,}02.10^1$	41

Electron microscopy of MW-ATO

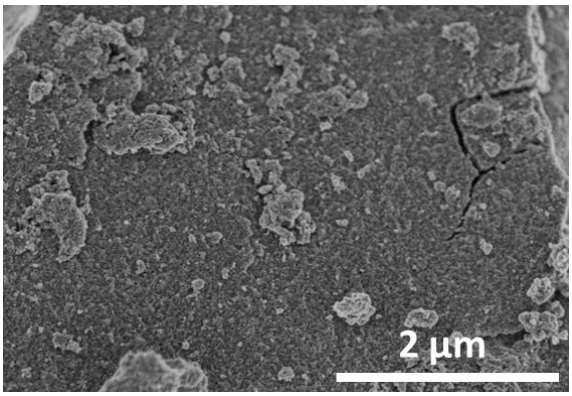

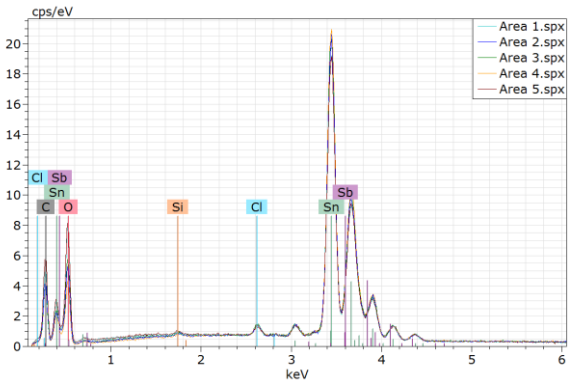

Figure S2. SEM-EDX of MW-ATO. The image represents a typical location for EDX.EDX-spectra were taken at a primary energy of 20 kV in random areas with a window size of 5 µm x 5 µm on different agglomerates (interaction depth: 2 µm) and confirm a homogeneous Sn:Sb-ratio of 95:5.

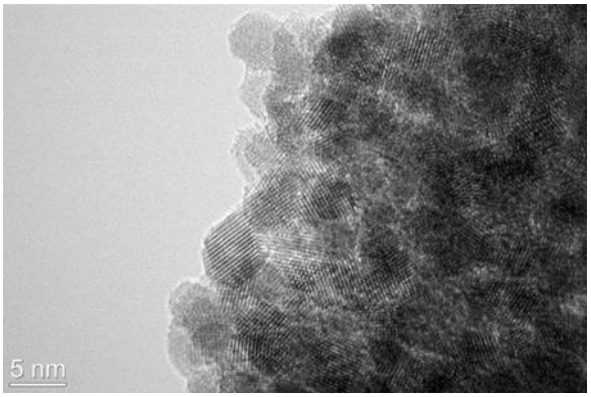

Figure S3. TEM-image of MW-ATO.

XRD of the Ir-loaded compounds

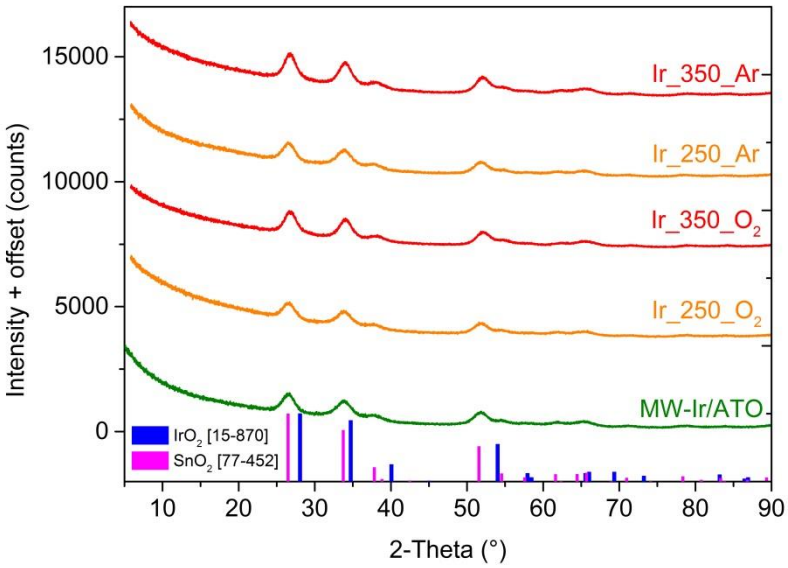

Figure S4. XRD of as synthesized MW-Ir/ATO (green line) and of thermal treatment products at 250°C (orange) and 350°C (red) under 100 mln min^{-1} of 21%-O_2/Ar or 100%-Ar.

Electrochemical testing

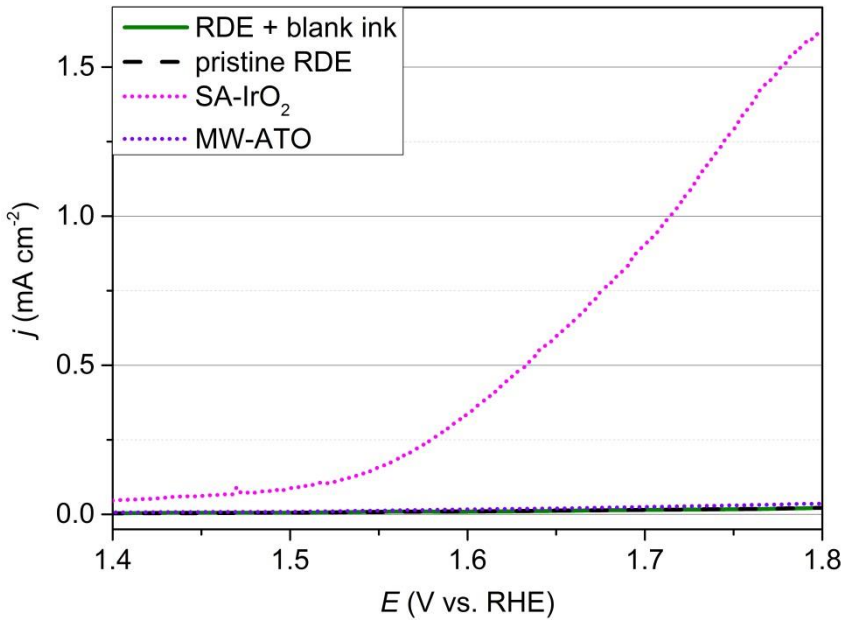

Figure S5. LSV of SA-IrO_2, MW-ATO, the pristine GC-RDE and the GC-RDE loaded with blank ink (no catalyst, only H_2O, iPrOH and Nafion).

TEM of MW-Ir/ATO

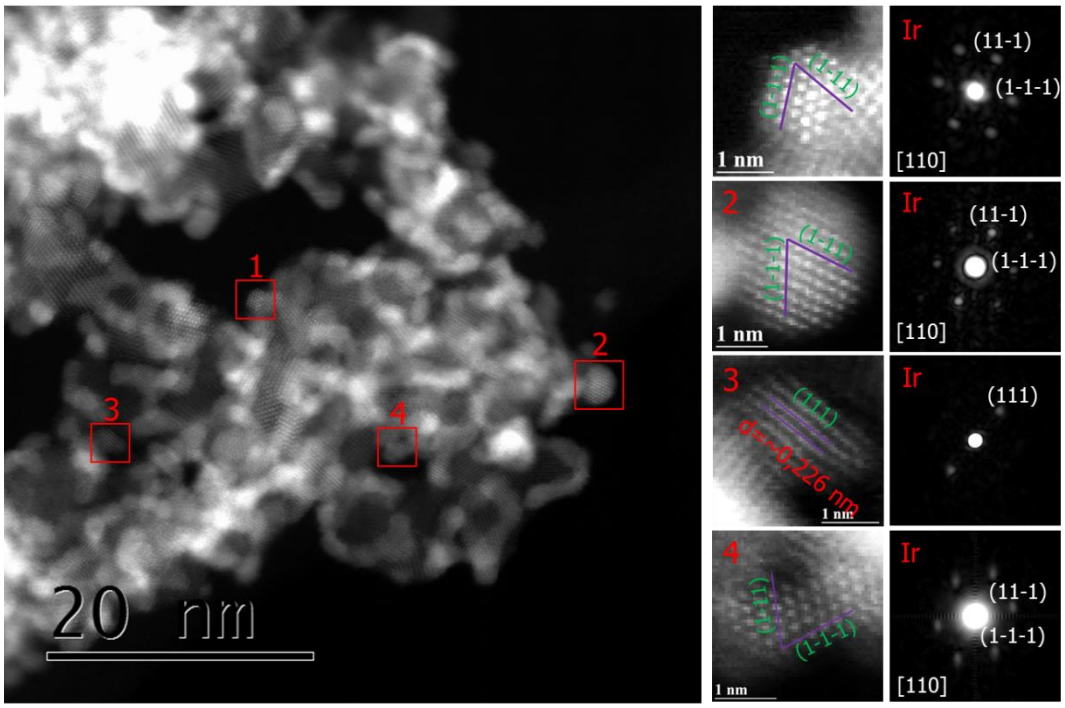

Figure S6. HAADF-STEM imaging of MW-Ir/ATO including Fast-Fourier-Tranformation of selected Ir-particles

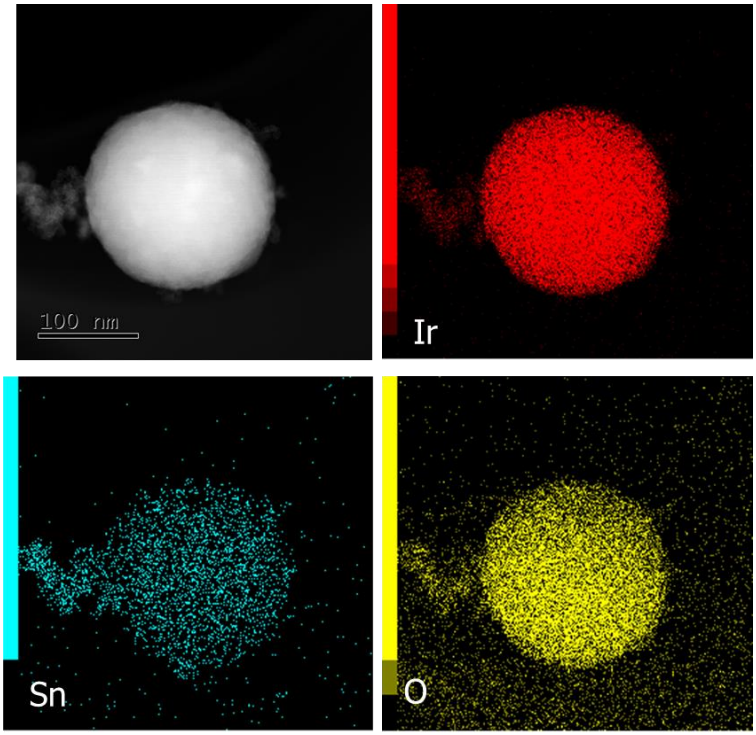

Figure S7. HAADF-STEM imaging of MW-Ir/ATO including EDX-based elemental mapping of one of the Ir/ATO-clusters found in MW-Ir/ATO

TGMS curves for the decomposition of MW-ATO and MW-Ir/ATO

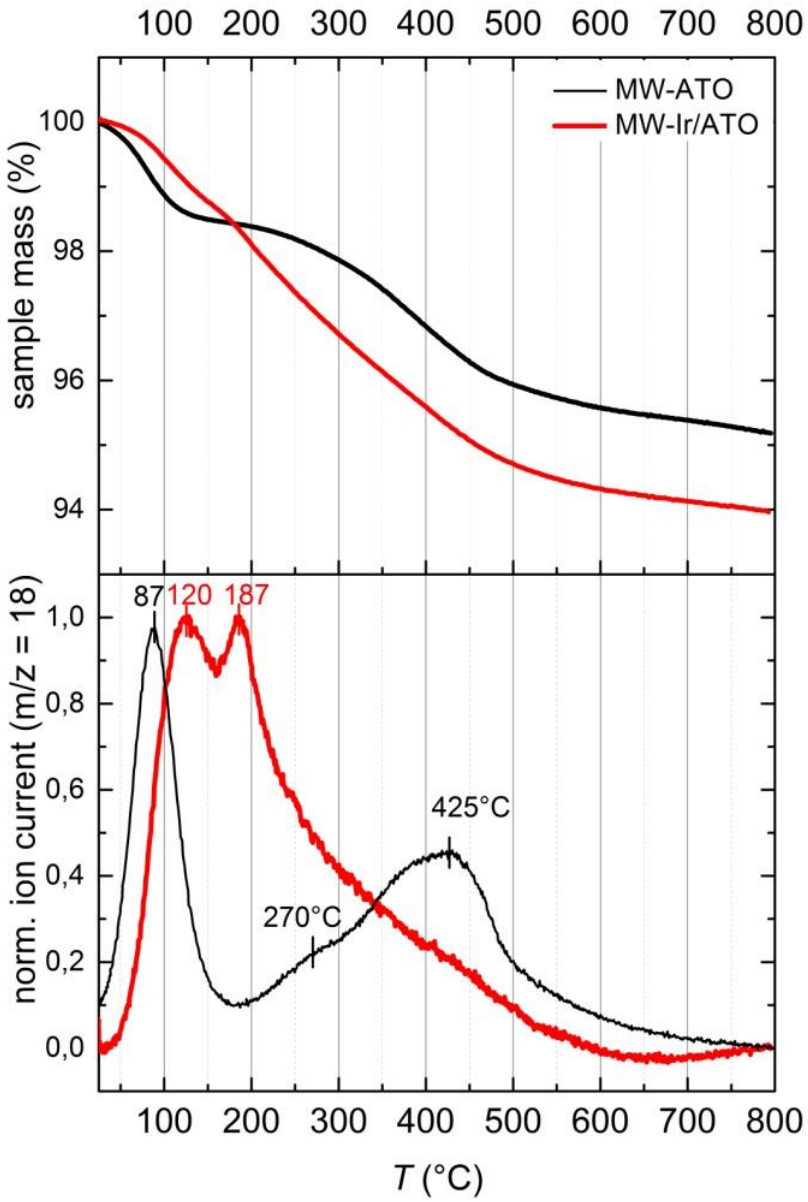

Figure S8. TG-MS curves for the decomposition of MW-ATO and MW-Ir/ATO under 21%-O_2/Ar (100 mln.min-1).

TPR-profiles of MW-ATO and SA-IrO_2

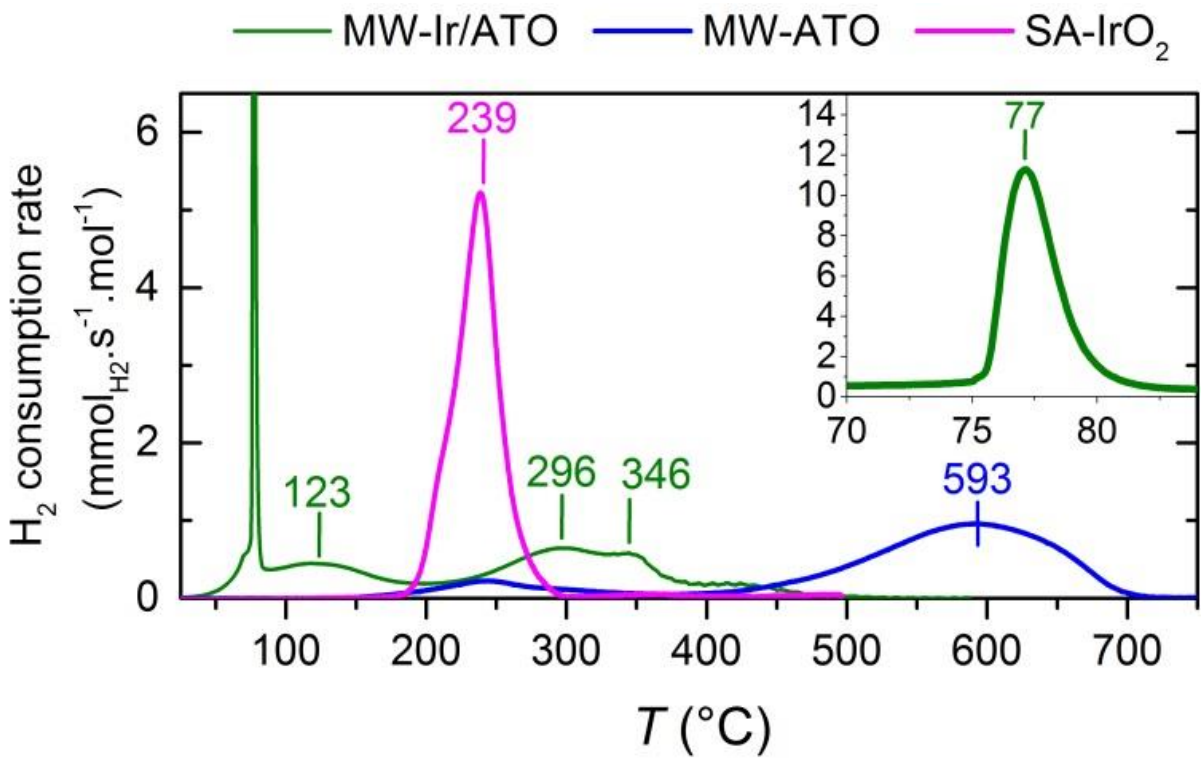

Figure S9. TPR-profiles of MW-ATO, MW-Ir/ATO and SA-IrO_2. The significant low-temperature reduction feature of MW-Ir/ATO is shown in the inset.

XRD of MW-Ir/ATO after TGMS

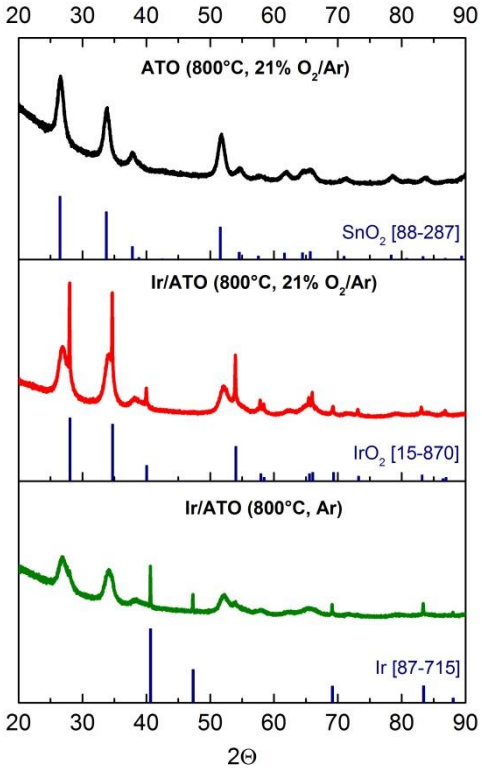

Figure S10. XRD the calcination products of the MW-ATO-support and the loaded MW-Ir/ATO after thermogravimetric analysis in oxidative (21%-O_2/Ar) and inert (Ar) gas streams.

Temperature-programmed reduction (TPR)

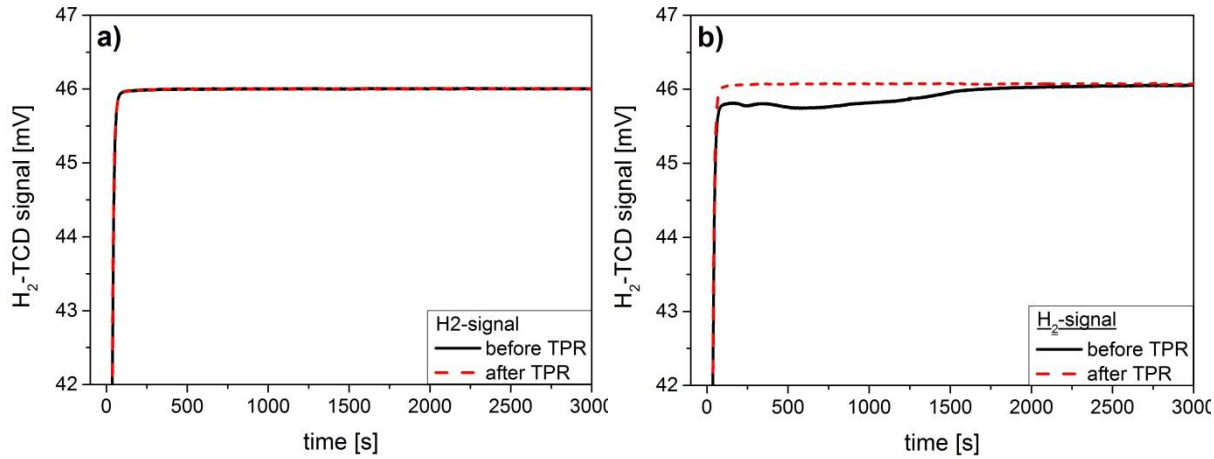

Figure S11. Time-dependent hydrogen signals detected via the Thermal Conductivity Detector (TCD) during the switch from a 100% Ar to a 5% H2/Ar gas stream (80 mL min^{-1}) before (dark line) and after the TPR (red dashed line) for MW-ATO (Fig. S11.a) and MW-Ir/ATO (Fig. S11.b).

Nominal sample composition and oxidation state

We pose the formal composition (1) of MW-Ir/ATO and Ir_(250/350)_O_2/Ar as :

$$(IrO_x)_{0.33}(Sb_{0.05}Sn_{0.95}O_2)_{0.67}(H_2O)_z \quad (1)$$

H_2O present in formula (1) correspond to the chemisorbed and physisorbed water present in a sample. The H_2O-content z of the sample is linked to the total water mass fraction $x_{m,H2O}$ via equation (2), where M is the molar mass of the compound.

$$x_{m,H_2O} = \frac{18z}{M} \quad (2)$$

$x_{m,H2O}$ is determined from TGMS by considering that the mass changes observed are mostly related to water removal. For MW_Ir/ATO, $x_{m,H2O}$ is determined from the total mass loss observed during TGMS to 800°C (Fig. 4). For the thermally treated samples, $x_{m,H2O}$ was determined using a stepwise TGMS experiment simulating the thermal treatment of MW-Ir/ATO (Fig. S10). In this experiment, the observed mass loss at the end of each step is assigned to water removal and substracted from $x_{m,H2O}$ in MW-Ir/ATO, yielding the remaining water content in the thermally treated sample.

The molar mass of the compounds is given according to (1) by (3):

$$M = 16 \times (2 \times 0.67 + 0.33\,x) + 0.33 \times 192.22 + 0.67 \times 0.05 \times 121.75 + 0.67 \times 0.95 \times 118.71 + 18\,z \quad (3)$$

The parameter x in M is not known. For this purpose, we use TPR. In TPR, the reduction of Ir-oxide and ATO will proceed respectively via schemes (4) and (5).

$$IrO_x + x\,H_2 \rightarrow Ir + x\,H_2O \quad (4)$$

$$(Sn_{0.95}Sb_{0.05})O_2 + 2\,H_2 \rightarrow (Sn_{0.95}Sb_{0.05}) + 2\,H_2O \quad (5)$$

As a result, the overall H_2-consumption n_{H2} based on the general formula (1) can be linked to x via equation (6), where m_s is the sample mass used in the TPR-experiment.

$$n_{H_2} = (0.33\,x + 2 \times 0.67) \times \frac{m_s}{M} \quad (6)$$

The combination of equations (2), (3) and (6) yields the analytical solution (7) for x and (8) for z.

$$x = \frac{1.34\,m_s\,(1 - x_{m,H_2O}) - 164.51\,n_{H_2}}{5.28\,n_{H_2} - 0.33\,(1 - x_{m,H_2O})} \quad (7)$$

$$z = \frac{x_{m,H_2O}}{18\,(1 - x_{m,H_2O})} \times \left[164.51 + 5.28\,\frac{1.34\,m_s\,(1 - x_{m,H_2O}) - 164.51\,n_{H_2}}{5.28\,n_{H_2} - 0.33\,(1 - x_{m,H_2O})}\right] \quad (8)$$

Eventually, the average oxidation state of Ir given by 2*x* can be calculated along with the parameters x, z and M listed in Table S2.

Table S2. Parameters used to determine sample composition and resulting oxidation states

Sample	**m_s (mg)**	**$x_{m,H2O}$ (%)**	**x**	**z**	**M (g mol^{-1})**	**Avg. oxidation state of Ir**
MW-Ir/ATO	31.1	5.9	1.64	0.6	183.96934	3.28
Ir_250_O_2	19.9	2.2	1.45	0.22	176.03614	2.9
Ir_350_O_2	18.5	1.1	2.03	0.11	177.20854	4.06
Ir_250_Ar	31.6	1.8	1.5	0.18	175.67014	3
Ir_350_Ar	17.5	0.8	1.26	0.08	172.60294	2.52

OER-performance after thermal treatment

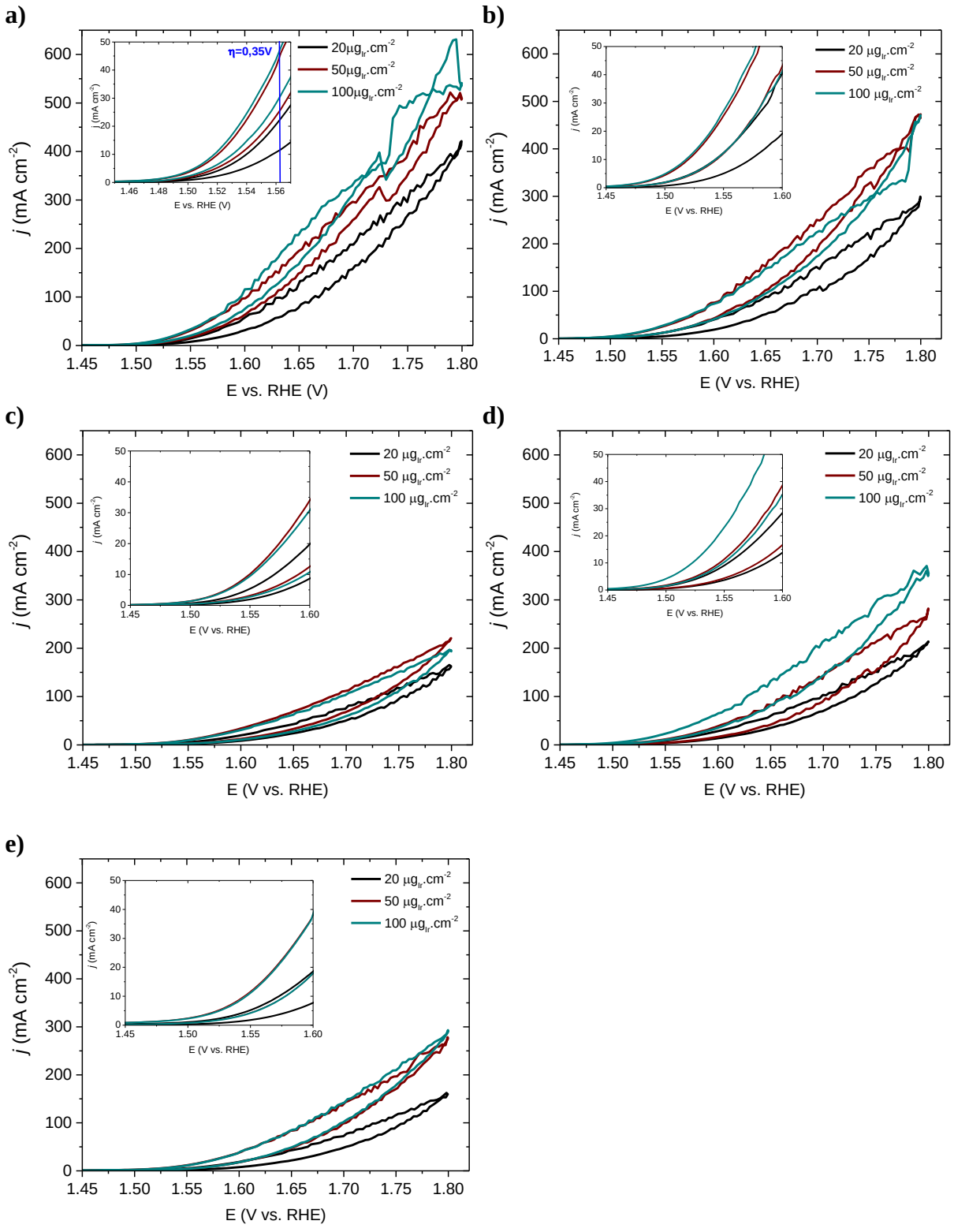

Figure S12. LSV-based activity test for three loadings at 20, 50 and 100 μg_{Ir} cm^{-2} a) MW-Ir/ATO b) Ir_250_O_2, c) Ir_350_O_2, d) Ir_250_Ar, e) Ir_350_Ar.

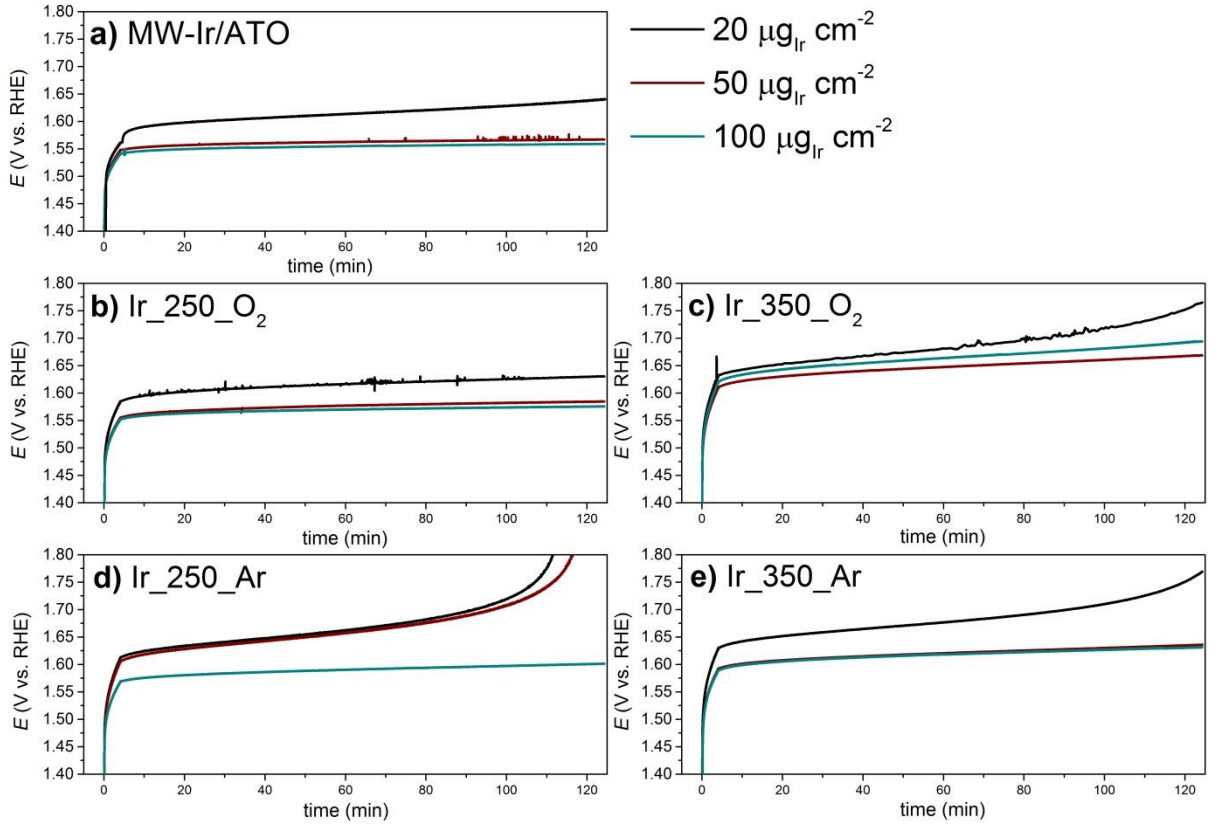

Figure S13. Stability-investigation of MW-Ir/ATO (a)) and its thermally treated products (b) Ir_250_O_2, c) Ir_350_O_2, d) Ir_250_Ar and e) Ir_350_Ar) in a chronopotentiommetric study for 2h at 10 mA cm^{-2}

Time-resolved behavior of Ir_350_O_2 under the electron beam

In some regions of Ir_350_O_2, we detected large portions of bare rutile-type ATO-support, which initially showed no birght spots assigned to metallic Ir-particles. However brighter contrast on the outer shell of ATO-particles, as shown in Fig. S14 suggests that the ATO support is covered with a thin Ir-layer in the same rutile-type structure. This corresponds to IrO_2-rutile. The time-dependent *in-situ* STEM observation of the same spot clearly showed that under beam irradiation, metallic Ir-particles blossomed in a matter of minutes where such brighter contrast could initially be observed. This indicates that the suspected thin IrO_2-layer is being reduced to Ir^0. IrO_2 has usually been described as stable under the electron beam. At 350°C, we are probably still in presence of a highly defective, partially hydroxylated IrO_2-type phase. The transition towards IrO_2 after treatment at 350°C however explains our ability to observe the reduction to Ir^0 under electron irradiation as the Ir-phase in Ir_350_ O_2 is closer to beam-stable IrO_2. Due to the difficulty of assigning phases formed or modified by the electron beam, the Ar-treated samples were not studied using STEM.

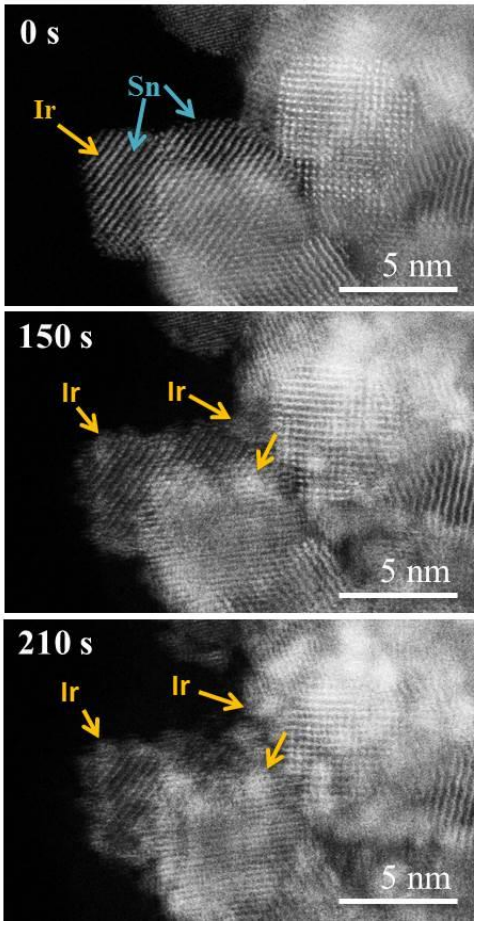

Figure S14. *In-situ* STEM observation of Ir_350_O_2 over 210s showing the evolution of sample morphology under the electron beam. The ADF-STEM imaging allows to relate contrast changes to heavier (brighter) Ir- or lighter (darker) Sn-atoms. Time-resolved imaging reveals the morphological changes of the Ir-phase under the beam.

TG-analysis of the stepwise calcination of MW-Ir/ATO

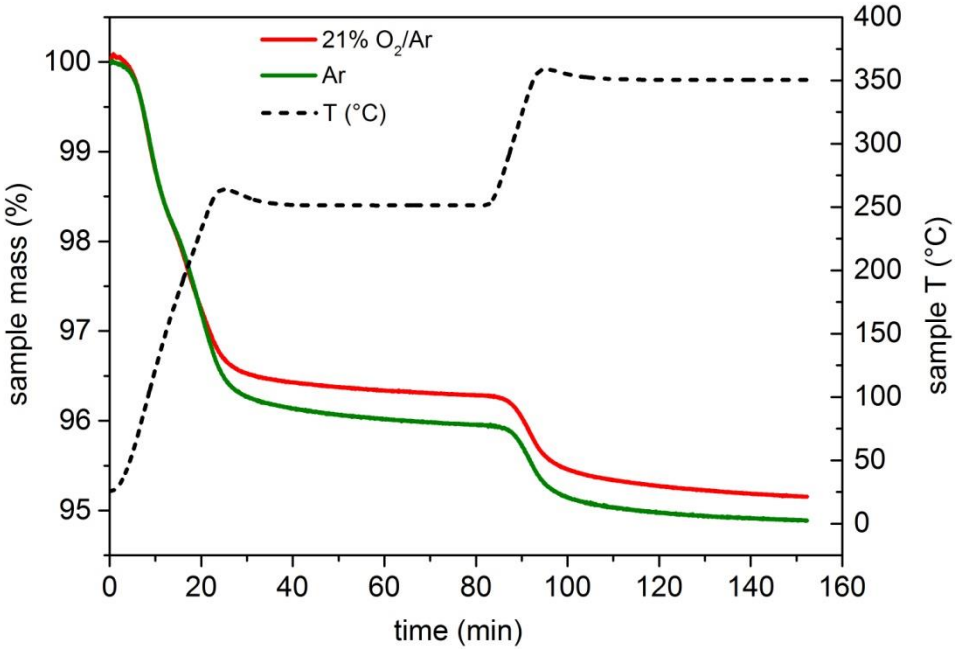

Figure S15. Thermogravimatric analysis of the stepwise annealing of MW-Ir/ATO in Ar and 21%O_2/Ar (100 mL min^{-1}) at 250°C and 350°C for 1h.

DRIFTS

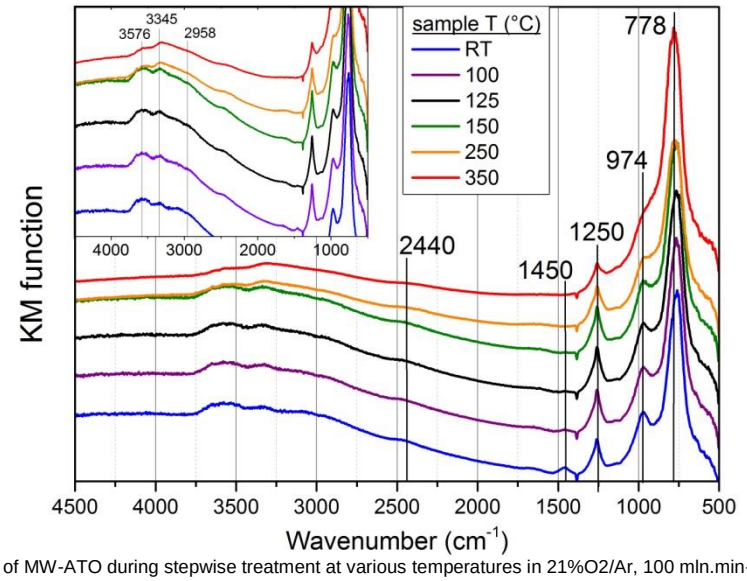

Figure S16. DRIFTS study of MW-ATO during stepwise treatment at various temperatures in 21%O2/Ar, 100 mln.min-1. Kubelka-Munck transformation of the reflectance spectra (left) and corresponding difference spectra between said temperature and 100°C (right).

In Figure S16, the feature located at approx. 1450cm^{-1} and disappearing at 125°C might be attributed to a unidentate carbonate species adsorbed on MW-ATO during the synthesis and originating from atmospheric CO_2 dissolved during the synthesis. Features at 1250 and 974 cm^{-1} can in turn be assigned to the vibration of hydroxyl-tin bonds according to the literature[1]. The diminution of these features at 250 and 350°C is in agreement with the hydroxyl decomposition profile observed in TGMS. Weak peaks in the 3650-32500 cm^{-1}-region can be assigned to more or less H-bonded hydroxyl groups. Additional broad feature around 2958 cm^{-1} might be assigned to C-H stretching frequencies from carbon impurities adsorbed on the surface of the sample. The strong contribution between 760 and 778 cm^{-1} is assigned to O-(Sn/Sb)-O, (Sn/Sb)-O-(Sn/Sb) and other lattice vibrations. In the literature these features are usually being observed at lower wavenumbers in the 600-660 cm^{-1}-range.[1-2] The important difference can be explained by varying tin doping levels as well as important differences in particle-sizes and -shapes, which have significant influence on peak positions.[3] Most FTIR-studies are being performed on ATO-films, in contrast to our 5 nm-particles. The observed increasing intensity of lattice features in the DRIFTS-spectra of MW-ATO is in line with an increasing crystallinity of the ATO upon calcination.

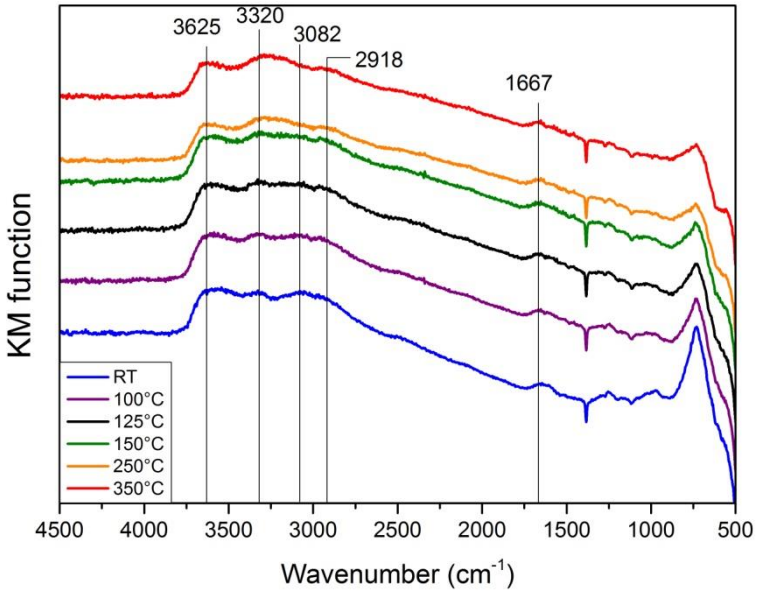

Figure S17. DRIFTS study of MW-Ir/ATO (Kubelka-Munck transformation of the reflectance spectra) during stepwise treatment at various temperatures in 21%O2/Ar, 100 mL min^{-1}.

Advanced electrochemical sample evaluation

MW-Ir/ATO and Ir_250/350_Ar/O_2 were subjected to a thorough screening procedure designed to yield a series of key performance indicators representative of OER-performance. The uncompensated ohmic resistance was determined via electronic impedance spectroscopy (EIS) using a high-frequency impedance measurement at open circuit potential (E_{oc}) (4 measurements, 100kHz, 20mV amplitude) and used by the EC-Lab software to automatically compensate for the ohmic drop in all following measurements. The electrode potential was first ramped to 1V vs. RHE (5 mV s^{-1}). The subsequent step assesses the initial OER-activity and consists of linear sweep voltammetry (LSV) from 1 to 1.8 V vs. RHE and back to 1 V vs. RHE (5 mV s^{-1}). In order to account for possible changes in the electrolyte, the uncompensated ohmic resistance is then measured again via EIS at E_{oc}. The following step is designed to test catalyst stability under relevant OER-conditions using a chronopotentiommetric (CP) measurement of the anode potential required to maintain constant current densities of 10 mA cm^{-2}. The target current density is reached via a galvanodynamic ramp of 10 µA cm^{-2}. After the CP-measurement, another LSV-measurement was performed in order to assess loss in activity over the 2h-CP-scan. This procedure is repeated for each compound with three different loadings (20, 50 and 100 μg_{Ir} cm^{-2}) in order to ensure some statistical certainty on the results with the additional advantage of providing information if the catalyst operates under kinetic control or whether mass-transfer/utilization effects come into play.

FHI-database references

Table S2. FHI-database ID-# of the samples reported in the present paper

Sample	FHI-database ID-#
MW-ATO	18966
MW-Ir/ATO	19527
Ir_250_O_2	22132
Ir_350_ O_2	22133
Ir_250_Ar	22134
Ir_350_Ar	22135
SA-IrO_2	20288
AA-IrO_x	20233

References

[1] J. Zhang, L. Gao, *J. Solid State Chem.* **2004**, *177*, 1425.
[2] R. Scipioni, D. Gazzoli, F. Teocoli, O. Palumbo, A. Paolone, N. Ibris, S. Brutti, M. A. Navarra, *Membranes* **2014**, *4*, 123.
[3] M. Ocaña, C. J. Serna, *Spectrochimica Acta Part A: Molecular Spectroscopy* **1991**, *47*, 765.